Atmospheric transport of subsurface, sporadic, time-varying methane releases on Mars

Orkun Temel [a,b], Özgür Karatekin [b], Elodie Gloesener [b,c], Michael A. Mischna [d] and Jeroen van Beeck [a]

[a] *von Karman Institute for Fluid Dynamics, Rhode-St-Genese, Belgium*

[b] *Royal Observatory of Belgium, Brussels, Belgium*

[c] *Université catholique de Louvain, Louvain-la-Neuve, Belgium*

[d] *Jet Propulsion Laboratory, California Institute of Technology, Pasadena, California, U.S.A*

Number of pages: 50

Number of tables: 4

Number of figures: 13

Preprint submitted to Icarus *30 January 2019*

Proposed Running Head:

Modelling of the methane releases from Mars' subsurface

Please send Editorial Correspondence to:

Dr. Orkun Temel

von Karman Institute for Fluid Dynamics

Environmental and Applied Fluid Dynamics Department

Waterloosesteenweg 72, Rhode-St-Genese, B-1640, Belgium

Email: orkun.temel@vki.ac.be

Phone: +32 470 242 470

ABSTRACT

This study is devoted to the general circulation modelling (GCM) of methane transport in the Martian atmosphere. A localized source originating from a near-subsurface methane reservoir is considered in the GCM simulations, which are performed with a modified version of the Weather Research and Forecasting (WRF) model, MarsWRF. The localized strength of a methane source varies with time, based on a 1-D near-subsurface diffusive transport. Time-varying surface release scenarios are also compared with an instantaneous release scenario. After release from the surface, the methane transport is investigated in the GCM as a passive scalar over time scales varying between 15 and 60 days, much shorter than the photochemical lifetime. Different emission scenarios of various duration and source intensity, as well as multiple locations with different elevation and terrain complexity are considered, to reproduce the substantial concentrations of methane (up to 50 ppb) observed in the northern hemisphere of Mars in 2003 (Mumma et al., 2009). Among the scenarios considered, the observations are reproduced best for an emission scenario of 45 sols duration, during which a total amount of about 90,000 metric tons of methane is released. The results reveal that observed Mars methane plumes in the northern hemisphere of Mars by Mumma et al. (2009) can be reproduced using a localized, time-varying methane source, consistent with a near surface methane reservoir.

Keywords: Mars, atmosphere; Mars, surface; Atmospheres, dynamics; Meteorology; General circulation modeling

1 Introduction

In the past decades, methane (CH_4) concentrations in the Martian atmosphere have been reported several times by different teams. One of the first methane detections was by Krasnopolsky et al. (2004) using ground-based facilities, while Formisano et al. (2004) detected methane from Mars orbit with the Planetary Fourier Spectrometer (PFS) on-board the Mars Express spacecraft. Both studies observed a similar average methane mixing ratio of approximately 10 parts per billion by volume (ppbv or ppb). Later, PFS observations with better global coverage evidenced a non-uniform distribution of methane concentrations in the atmosphere, suggesting the presence of local sinks or sources (Geminale et al., 2008). In addition to the spacecraft and Earth-based observations, in situ measurements of atmospheric methane have been made at Gale crater since 2012 using the Tunable Laser Spectrometer (TLS) of the Sample Analysis at Mars (SAM) instrument suite on the Curiosity rover. From the first TLS measurements covering a 20-month period, Webster et al. (2015) reported background levels of approximately 0.7 ppb and elevated levels up to 7.2 ppb, which suggests episodic releases of methane into the planet's atmosphere. A more recent observation by the Curiosity rover, covering a 5-year period, showed background levels of methane around 0.41 ppbv with a seasonal variation from 0.24 to 0.65 ppbv at the Gale crater (Webster et al., 2018).

The most comprehensive ground-based study was done by Mumma et al. (2009), hereafter M09. They provided evidence for substantial methane plumes using ground-based infrared spectroscopic techniques. In particular, the methane plumes observed by M09 during the northern summer on Mars ($L_S = 155.0°$) had mixing ratios of up to 50 ppb. The methane plume was detected in a longitudinal range of 37-83° E and centered on the equator. The mean methane mixing ratio was about 33 ppb (120 mol km^{-2}), and the plume contained 1.86 $\times$ 10^7 kg, or 19,000 metric tons of methane. The M09 observations were performed over different time periods and locations and suggested local source regions near the equator and possible temporal variations in the source strength. One of the major outcomes of M09 was the surprisingly rapid destruction of methane, which could not be explained by the known photochemistry of Mars' atmosphere (Lefèvre and Forget, 2009).

While the presence of methane on Mars and M09 observations were challenged (Zahnle et al., 2011; Zahnle, 2015), its implications for early Mars and habitability make it essential to understand its potential origin and evolution. Similar to Earth, methane on Mars could be produced by biotic or abiotic processes. It has been suggested that methane could be generated on Mars, today, by subsurface microbial ecological systems, similar to those discovered on Earth (Boston et al., 1992). Alternatively, early Martian life may have survived in aquifers deep below the permafrost (Weiss et al., 2000). Methane can also be produced abiotically as the result of ongoing or past geological processes including low-temperature alteration of Martian rocks (Lyons et al., 2005), comet impacts (Kress and McKay, 2004), and Fischer-Tropsch Type (FTT) reactions where H_2 reacts with CO_2 in the presence of a metal catalyst (Oehler and Etiope, 2017). The H_2 necessary for the FTT reactions can be produced by several processes and, notably, by serpentinization (Oze and Sharma, 2005). Regardless of its generation process on Mars, the methane produced today or in the past can be trapped in subsurface reservoirs, of e.g., clathrate hydrates (Chastain and Chevrier, 2007; Chassefière, 2009; Lasue et al., 2015) or zeolites (Holmes et al., 2015; Mousis et al., 2016). While isolated from the atmosphere, these reservoirs can remain stable for long time periods (Mousis et al., 2013, 2016) and the sporadic release of methane could be associated with their destabilization following sudden changes in environmental conditions (Kite et al., 2017; Elwood Madden et al., 2007; Mousis et al., 2013; Root and Elwood Madden, 2012).

As presented in Table 1, several GCM studies modeling the surface release of methane and its subsequent evolution in the atmosphere have been published following the M09 observations; Lefèvre and Forget (2009) investigated methane destruction timescales using a GCM with photochemical model for emission scenarios of 60 and 120 sols (one sol is a Martian day) with a uniform release rate. In their optimal scenario, they showed that in order to reproduce local methane enhancements similar to those observed by M09, an atmospheric lifetime of less than 200 days is required over which 150,000 metric tons of methane needs to be emitted at a constant rate. The existence of such a fast loss in the Martian atmosphere is difficult to reconcile with the observed distribution of other trace gas species (Lefèvre and Forget, 2009). Mischna et al. (2011) sought to identify the source location of the observed atmospheric M09 methane signals under reasonably realistic atmospheric conditions. Their results suggested that M09 observations can be reproduced best if the release occurred just before the time of observation, no more than 1-2 sols earlier, and if this release were nearly instantaneous rather than a slow, steady emission. More recently, by using point and regional emissions with a constant release rate over 30 sols, Holmes et al. (2015) examined the time evolution of methane in the atmosphere starting from an observed plume of methane, consistent with that reported in M09, while Viscardy et al. (2016) and Holmes et al. (2017) investigated the vertical distribution throughout the atmosphere, including the formation of layers, during the first weeks after the release by using instantaneous and temporally uniform releases. Although the choice of source locations were inspired by M09, the actual amount of emitted gas was not considered critical by Viscardy et al. (2016) as their focus was on the qualitative aspects of the dispersion of the gas throughout the atmosphere.

In this study, our goal is to reproduce, closely, the observed methane distribution by M09 and to propose a methodology that can constrain its source and emission conditions. Consistent with M09 analysis, we use different local source regions near the equator and consider temporal variations in the source strength. Therefore, not only the effect of emission duration and strength but also the effect of topography on the transport of a methane plume are investigated. Previous studies have assumed instantaneous or sustained surface emissions with a constant release rate. Here, we use methane emission scenarios consistent with the destabilization of shallow subsurface reservoirs and subsequent methane diffusion through the soil which results in time variable source strength. Various emissions from different locations over various temporal scales are considered. The resulting atmospheric methane concentrations are compared with M09 observations at L_S=155°. Remembering that the joint ESA/Roscosmos ExoMars Trace Gas Obiter (TGO) mission is searching for methane within the Mars atmosphere by limb and nadir measurements, both horizontal and vertical distributions throughout the atmosphere are investigated.

The paper is organized as follows. Section 2 provides general information about the MarsWRF GCM, while Section 3 describes the emission scenarios and the general settings for numerical simulations. This is followed by Section 4 where the temporal evolution of horizontal and vertical distributions of methane and comparison with the M09 observations are provided. Finally, Section 5 and Section 6 present the discussion and our conclusions.

Table 1

Methane transport studies with global circulation models, including this work.

Ref.	GCM model	GCM resolution	Methane emissions
Lefèvre and Forget (2009)	LMD GCM with photochemistry	3.75 x 5.625 32 levels (120 km)	point sources constant release rate
Mischna et al. (2011)	MarsWRF no photochemistry	1.25 x 1.25 40 levels (80 km)	point + regional sources instantaneous release
Holmes et al. (2015)	LMD GCM (UK) no photochemistry	5.0 x 5.0 32 levels (100 km)	point + regional sources constant release rate
Viscardy et al. (2016)	GEM-Mars no photochemistry	4.0 x 4.0 102 levels (150 km)	point sources instantaneous + constant release rate
Holmes et al. (2017)	LMD GCM (UK) no photochemistry	5.0 x 5.0 35 levels (105 km)	point sources instantaneous + constant release rate
this study	MarsWRF no photochemistry	2.5 x 2.5 52 levels (80 km)	point sources time-varying release rate

2 MarsWRF global circulation model

MarsWRF, the GCM used in this study, is a multiscale atmospheric model bridging the gap between global and mesoscale models. It has the capability of nesting and a generalized map projection. MarsWRF atmospheric temperatures have been validated against TES observations (Lee et al., 2011) and surface pressure against Viking lander measurements (Guo et al., 2009) with excellent results. It was developed by adapting the Weather Research and Forecasting (WRF) model for Mars (Richardson et al., 2007; Toigo et al., 2012). Other versions are available for Titan, Venus and Pluto (McDonald et al., 2016; Lee et al., 2006; Toigo et al., 2015). The model is based on the classical terrain following modified-sigma coordinates of an Arakawa C-grid. The computational grid has been modified to work with nonconformal map projections. Based on an intercomparison study of different Mars GCMs to assess the capabilities of the existing models to provide realistic predictions in comparison to the observations, it was shown that MarsWRF is able to reproduce TES temperature data (Smith et al., 2001) with a high degree of similarity to the observations (Guo et al., 2009; Mischna and Wilson, 2008; Lee et al., 2009). Due to the importance of the temperature distribution on the local winds, the predicted surface temperature by MarsWRF is compared with TES temperature data (Smith et al., 2001) corresponding at the time period of interest, $L_S = [150°, 170°]$, as shown in Fig. 1.

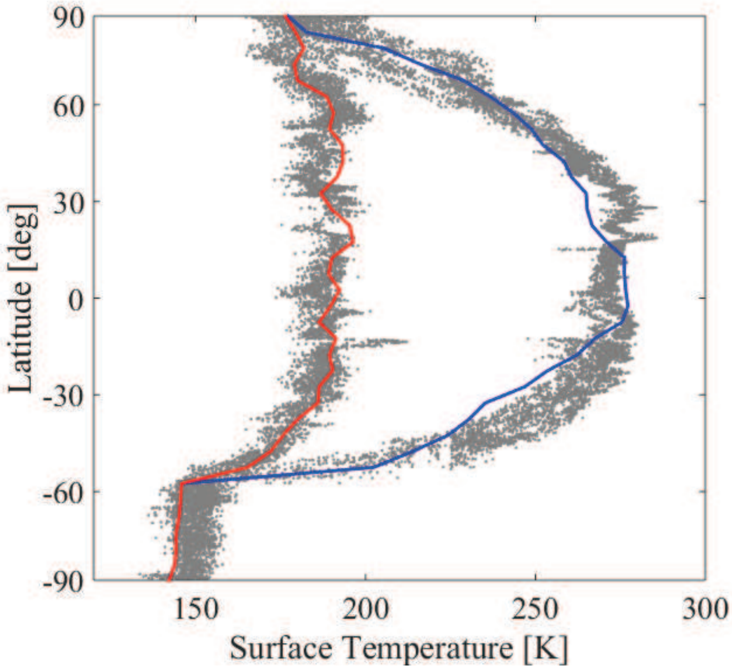

Fig. 1. Comparison of predicted surface temperature distribution with TES temperature dataset on 60° E, where the M09 observation is centered: Red solid line - predicted nighttime temperature (02:00 local time), blue solid line - predicted daytime temperature (14:00 local time), gray points - TES observations (Smith et al., 2001).

MarsWRF contains parameterizations of numerous physical processes and sub-grid schemes. These include water microphysics, a CO_2 cycle interacting with radiative heat transfer and prescribed time-varying spatial distribution of atmospheric dust. Atmospheric dust content may be prescribed, based on

TES observations, to represent a specific dust scenario, e.g., that observed by the Mars Global Surveyor. In this study, a dust scenario corresponding to the average of TES limb observations for Martian Year 24-27 is used. In addition, surface layer and planetary boundary layer schemes for the parameterization of turbulent fluxes within the boundary layer (Hong and Pan, 1996) are included as well. An additional passive scalar transport equation has been added to the governing equations to model the dispersion of the passive methane plume.

The model parameters are similar to those used previously by Mischna et al. (2011), to simulate the methane transport using MarsWRF. The details of the models parameters are given in the following section.

3 Methane emission scenarios

3.1 Source and subsurface transport

The origin, as well as the fate, of methane plume observed by M09 is not known. If methane is released sporadically from localized sources with time-variable intensity, as suggested by M09, the sources can be in the Martian subsurface. The deeper the methane source is located, the longer it takes for the gas to be transported through the soil into the atmosphere. Considering the fact that pure diffusion is a slow process, we only consider near-subsurface reservoirs so that the surface methane emission occurs in only a few tens of sols. Given these assumptions, methane emission rates are simulated as a function of time.

The methane, once released from the subsurface reservoir, is assumed to be transported to the surface by diffusion. The diffusion process depends on the pore size and the mean free path of the molecules diffusing through the soil. It can be modeled in two primary regimes: Fickian diffusion, also called normal diffusion and Knudsen diffusion, e.g., Welty et al. (2009). In Fickian diffusion, the pore radius is larger than 10x the mean free path of diffusing species, and collisions between gas molecules dominate. Knudsen diffusion occurs when the pore radius is less than one-tenth of the mean free path, and gas-wall collisions dominate. In the transition regime, when the mean free path is on the same order as the pore size, both Fickian and Knudsen diffusions have to be taken into account. Under the pressure conditions of Mars, the mean free path of methane is $\sim$10 μm, about the same order as the pore size, and the diffusion regime falls in the transition regime.

To model the diffusion of gases within the Martian subsurface, the porous medium is treated as a series of parallel cylindrical pores (Sizemore and Mellon, 2008) and a one-dimensional partial differential equation, similar to that of Stevens et al. (2017), taking into account Knudsen flow and molecular diffusion is solved with a Crank-Nicolson scheme. The gas phase pressure in pore spaces is calculated assuming a surface pressure of 610 Pa and using two cases for the pressure gradient: lithostatic and hydrostatic. However, the real pore pressure profile is generally more complex depending on how pores are connected and their saturation state (Max and Clifford, 2000). The boundary conditions in our 1D thermal model are chosen to be the surface temperature at the top and the surface heat flux at the bottom (19 mW m^{-2}), representing the present-day average value on Mars (Parro et al., 2017). The values for the subsurface parameters of the reference simulation are chosen to be representative of Mars-analog soils (Sizemore and Mellon, 2008) and are given in Table 2.

Table 2

Properties of the porous medium, used in the calculations of Fig. 2.

Parameter	**Value**
Porosity	0.4
Mean pore radius (μm)	10
Tortuosity	1.5
Volumetric heat capacity (J m^{-3} K^{-1})	1.28×10^6
Thermal inertia (J m^{-2} K^{-1} $s^{-1/2}$)	280

The transported methane is then released at the surface and the emission is assumed to occur over a period of 15 to 60 sols around solar longitude $L_S = 155°$. Similar emission durations have been used by previous studies (Lefèvre and Forget, 2009; Holmes et al., 2015, 2017; Mischna et al., 2011; Viscardy et al., 2016) in order to reproduce temporal and spatial variability in Mars methane observations.

Assuming atmospheric hydrostatic pressure in pore space, the sources must be located at 15, 22, 27, 31 m below the surface to allow for emission durations of 15, 30, 45 and 60 sols, respectively. If the other extreme, i.e., lithostatic pressure, is assumed, the source depths are about 4 times smaller to provide the same methane release rate profiles. In other words, reservoir depth and subsurface pressure are interchangeable unknowns.

For a total amount of methane of $\sim 1.86 \times 10^7$ kg as reported by M09, the time variable surface fluxes are presented in Fig. 2. As expected, the peak flux is higher and is reached sooner following initial release from a shallower source, which corresponds to a shorter emission duration. The emission profiles in Fig. 2 are similar and can be scaled to change the total amount of methane released in a given scenario as shown in the next section.

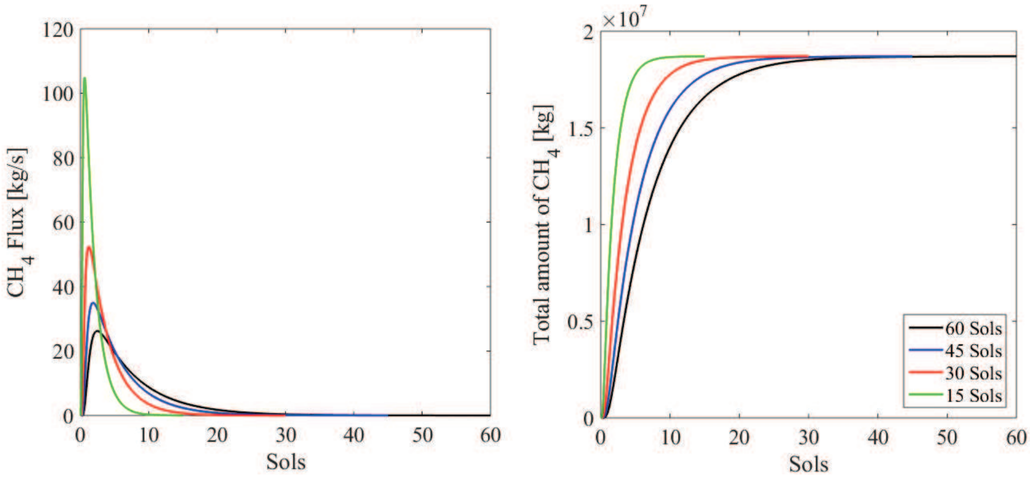

Fig. 2. Temporal evolution of methane flux and cumulative mass for different release durations. The total amount of methane release is 1.86 $\times 10^7$ kg corresponding to the local methane plumes observed by M09. If the release is not instantaneous from the region of M09 observations, a larger amount of methane is needed to match the observed local concentrations. Hence, in the GCM simulations, total amount is increased with emission duration, as shown in Table 3.

3.2 Release

Previous GCM simulations by Mischna et al. (2011) showed that in the beginning of the emission, the methane plume mostly remained within a narrow latitudinal range on the equator, failing to reproduce the M09 observations. Despite latitudinal mixing being enhanced over time, GCM simulations based on a localized source failed to predict the methane mixing ratio peak on the equator by using the total amount of methane suggested by Mumma et al. (2009).

Similar to Mischna et al. (2011), methane is released at the surface in a single grid cell of the model measuring 2.5° × 2.5° in latitude and longitude (~ 22,000 km^2, the emission area). However, the total amount of methane injected into the atmosphere during these periods is adjusted to match the important local maximum of up to 50 ppb observed in northern summer 2003 by M09 by modifying the rates shown in Fig. 2. The total amount of emitted methane for the four simulations is presented in Table 3. As mentioned by Lefèvre and Forget (2009), a considerably more intense source than observed by M09 is required in order to match the temporal and spatial variability of the methane plumes. The total amount of methane given in Table 3 is in quantitative agreement with Lefèvre and Forget (2009) where 150,000 metric tons of methane was emitted over 60 days at constant rate by a sporadic source in Syrtis Major to produce their best match to the M09 observations. Even though the methane peak reported in M09 observations on the equator can be reproduced by adjusting the total amount of methane, the latitudinal distribution of methane depends on the time elapsed since the emission was initiated. As noted before, within a short time period, the methane plume will not be sufficiently transported in the meridional direction. On the other hand, if this time period is larger than the emission duration, the methane concentration peak close to the longitudinal range where the emission is initiated, and close to the equator in our cases, would decrease so that it would require an even much larger amount of emitted methane. Therefore, the emission is initiated at a specific solar longitude such that more than 98% of the total amount of methane is emitted by $L_S = 155°$, when the M09 observations were made. More specifically, the emissions in our different scenarios start 24, 18, 12 and 6 sols before the M09 observations for the emission scenarios of 60, 45, 30 and 15 sols, respectively.

The atmospheric transport of methane is significantly affected by altitude and topographical features of the release area. The diverse emission sites consid-

Table 3

Methane emission duration and source strength.

Duration (sol)	Total amount of methane (kg)	Mean release rate (kg/s)	Observation time (sols)*
60 sols	1.24 x 10^8	24	24
45 sols	8.99 x 10^7	23	18
30 sols	5.55 x 10^7	21	12
15 sols	4.07 x 10^7	31	6

*Sols after initial release at M09 observations (L_S=155°) when 98% of the total amount of methane is emitted.

ered in this study are shown in Fig. 3 and are all located close to the equator, consistent with the M09 observations. Ten separate simulations are performed with the methane source placed within the Arsia Mons, Coprates, Sabaeous, Iapygia and Aeolis regions. The coordinates of these locations with their corresponding elevation are listed in Table 4, where Iapygia II corresponds to a previously studied region (Mischna et al., 2011).

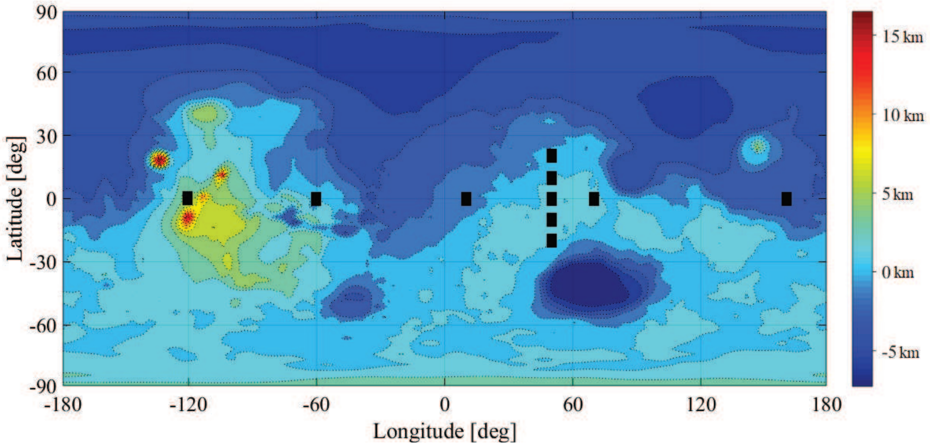

Fig. 3. Topography with the model's resolution and the emission locations listed in Table 4.

Table 4

Methane source locations considered in this study

	latitude, longitude	**MOLA elevation (km)**
Arsia Mons	(0° N, -120° E)	6.2
Coprates	(0° N, -60° E)	1.1
Sabaeous	(0° N, 10° E)	-0.7
Iapygia	(0° N, 70° E)	1.8
Iapygia II	(0° N, 50° E)	2.2
Iapygia II - S2	(20° S, 50° E)	1.8
Iapygia II - S1	(10° S, 50° E)	2.4
Iapygia II - N1	(10° N, 50° E)	1.2
Iapygia II - N2	(20° N, 50° E)	0.2
Aeolis	(0° N, 160° E)	-2.8

3.3 Atmospheric transport

The GCM simulations have been performed with a latitude x longitude resolution of 2.5° x 2.5° with 52 vertical levels (0 - 80 km). Considering the Courant-Friedrichs-Lewy criterion, the time step of the model is set to be 90 s. The integration and parameterization schemes, the horizontal eddy diffusivity and other model parameters are selected based on the previous GCM study of methane transport with MarsWRF (Mischna et al., 2011), except the polar filtering latitude that is set to 60° in our case. A methane chemical lifetime of

1000 sols and a 30-sol spin-up period are chosen, similarly to Mischna et al. (2011).

4 Results

Methane release scenarios described in section 3 are run with MarsWRF and compared with the M09 methane observations. First, we test the effect of emission duration or reservoir depth (see Table 3) at a given source location. We then investigate the sensitivity to the equatorial and latitudinal locations (Table 4) and the results are compared with an instantaneous emission scenario.

4.1 Methane emission duration

GCM simulations are performed using methane release rate scenarios with duration of 60, 45, 30 and 15 sols (see Table 3). In order to evaluate these emission scenarios, Iapygia II, the source location previously studied by Mischna et al. (2011) with an instantaneous emission scenario, is considered as the release area. This region, surrounding Terra Sabae and Syrtis Major where methane appeared notably localized in observations of M09, includes both Noachian- and Hesperian-age surfaces and a large range of spectral and morphologic units, such as linear ridge networks, that are found throughout the highlands (Mustard et al., 2007, 2009).

In Fig. 4, the latitudinal methane concentrations obtained for the different emission scenarios are compared with the M09 observations at $L_S = 155°$. The variations of methane mixing ratio with latitude are obtained by performing spatial average on the longitudinal range corresponding to the M09 observations, 32° - 82° E. Results obtained by Mischna et al. (2011) with the same GCM but assuming an instantaneous methane emission is included for comparison. The results of the instantaneous release case show a sharp peak at the equator since the methane plume is not transported far in the meridional direction. Moreover, it has been shown that the methane concentration falls below the observations after six sols (Mischna et al., 2011).

Contrary to the instantaneous release case, GCM simulations with a time-varying release scenario (see Fig. 2) provide a better mixing ratio poleward of 25° in both hemispheres. The methane emission scenario of 15 sols presents a slightly wider methane plume spread over a latitudinal range between 40° S and 45° N. For the emission scenario of 30 sols, the maximum difference between the observations and the computations is 15 pbb, whereas the instantaneous emission shows a maximum difference of 30 ppb. The results also illustrate that with a longer emission duration, the meridional transport of methane is enhanced. At the moment of the M09 observations, 98% of the total amount of methane has been released for each scenario implying that short emission scenarios have had less time to disperse methane through the atmosphere, as evidenced by the sharper distributions. The cases where the surface release is active during a longer time period are able to better reproduce the observed latitudinal dispersion. The best agreements with the observations are found using the methane emission scenarios longer than 30 sols, with a maximum difference of 10 ppb and 7 ppb for the emission scenarios of 45 sols and 60 sols, respectively.

As a result of the convective mixing, driven by the temperature gradients in the atmosphere, the methane will be lifted from the surface and dispersed

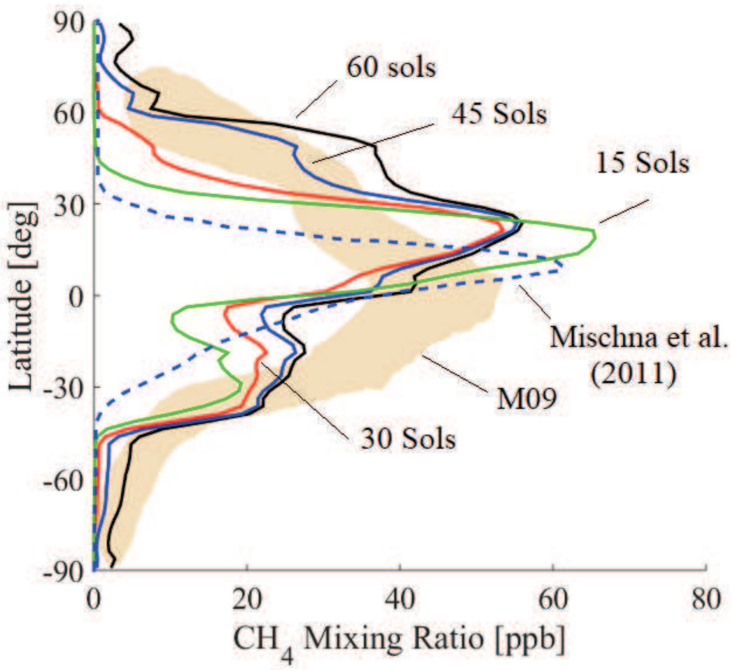

Fig. 4. Comparison of latitudinal methane concentrations for different emission scenarios from Iapygia II, with M09 observations at L_S =155°.

within the boundary layer rapidly. Therefore, the transport of methane mainly depends on the boundary layer winds, which we represent by the average winds in the lowermost atmosphere, on the first scale height. 20-sol average winds on the first scale height are presented in Fig. 5a. For an instantaneous release, the average winds on the first scale height, alone, are sufficient to interpret the atmospheric methane transport due to the fact the methane released from the surface will be rapidly lifted and distributed vertically up to the top of the planetary boundary layer. However, in the case of a continuous release, the effect of surface and near-surface layer winds on the transport of methane will be persistent during the surface emission around the emission site as a result of the time-varying release. Therefore, the averaged winds at 1 km altitude, corresponding to roughly the lowest 10% of the boundary layer, are also presented in Fig. 5b.

The contours of column integrated methane mixing ratio of the four different emission scenarios for the Iapygia II (0° N, 50° E) case are presented in Fig. 6. For all emission scenarios, the highest methane abundance is obtained in the Arabia quadrangle, north-west of the emission site, consistent with the winds blowing from south-east to north-west in the Iapygia region (see Fig. 5). The lifted methane plume is then transported zonally by the boundary layer winds and the effect of mid-latitude jets manifest themselves on the latitudinal variation of the methane plume. The effect of topography is seen in Fig. 6d by the low concentration zone around Tharsis Montes. Even though the methane plume is dispersed along the equator, methane is not yet convected vertically high enough to pass over the Tharsis region, where the elevation is up to 15 km.

Among the emission scenarios presented in Fig. 4 and Fig. 6, the emission scenario of 45 sols seems to be the optimum scenario in terms of balancing the meridional transport and total amount of methane. Therefore, in the following sections, several simulations are performed to investigate the sensitivity of the methane transport to emission location with this scenario. The quantitative comparison between predictions and the M09 observations is presented in Table 5 in terms of a 'hit rate' for model success. Hit rate is defined as $R = \frac{\sum_{i=1}^{n} N_i}{n}$, where n is the number of model points on a latitudinal range and N_i is 1 if $N_{min} < N_i < N_{max}$ and 0 otherwise; N being the predicted concentration at a given latitude and N_{min} and N_{max} being the minimum and maximum concentration reported by the M09 observations at the same latitude. In other words, it is defined as the fraction of the predicted concentration curve that falls within the min/max bounds reported by M09, shown as the shaded region in Fig. 4.

Table 5

Intercomparison of emission scenarios to reproduce the M09 observations

Emission scenario	**Hit rate [%]**
Instantaneous	13.1
15 sols	14.8
30 sols	21.3
45 sols	59.0
60 sols	52.5

4.2 Sensitivity to equatorial location

Given the importance of local and global circulation for the methane dispersion near Iapygia II, we consider methane emissions at different locations on the equator. These are indicated in Fig. 3 and described in Table 4. GCM simulations are performed for six equatorial methane emissions in the Arsia Mons, Coprates, Sabaeous, Iapygia, and Aeolis regions. Table 4 gives five more locations away from the equator, which are considered in the next subsection. We consider only the 45-sol emission scenario and investigate the influence of elevation and wind field on the methane dispersions simulated by the GCM.

The contours of the global column integrated methane concentration at $L_S = 155.0°$ for the different surface emission locations are given in Fig. 7

The atmospheric transport of the methane plume is highly dependent on the source location. Topography not only affects the surface and near-surface layer winds but also the boundary layer winds as shown by Petrosyan et al. (2011), and the elevation of the source location is also important as it defines the timescale over which the methane plume will be convected with the general circulation. As presented in Fig. 7, there are similarities with the zonal trans-

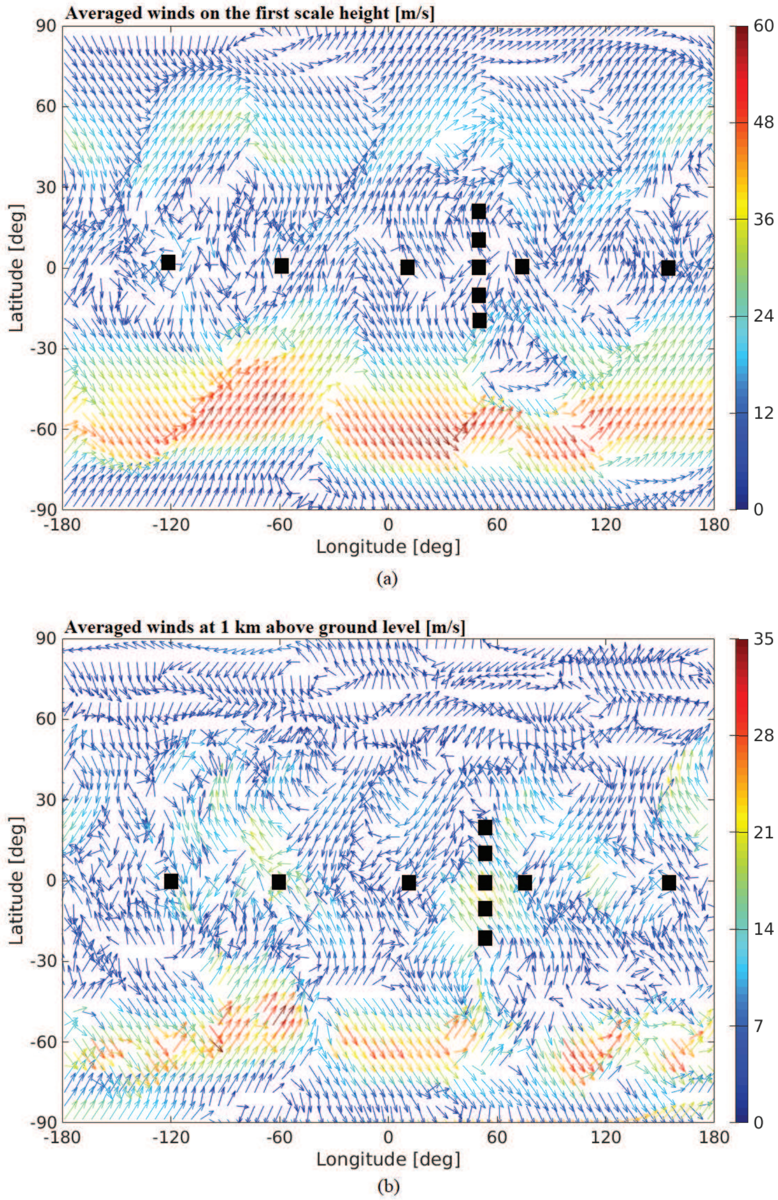

Fig. 5. Wind velocity (m/s) averaged over 20 sols around the M09 observation period, L_S = 145-155° (a) on the first atmospheric scale-height and (b) at 1 km above ground, methane source locations are indicated, see Table 4.

port of methane for different locations, as the zonal transport is mainly driven by the boundary layer winds presented in Fig. 5a. Their impact is reflected in every case to some degree. However, the latitudinal mixing is quite different for each location.

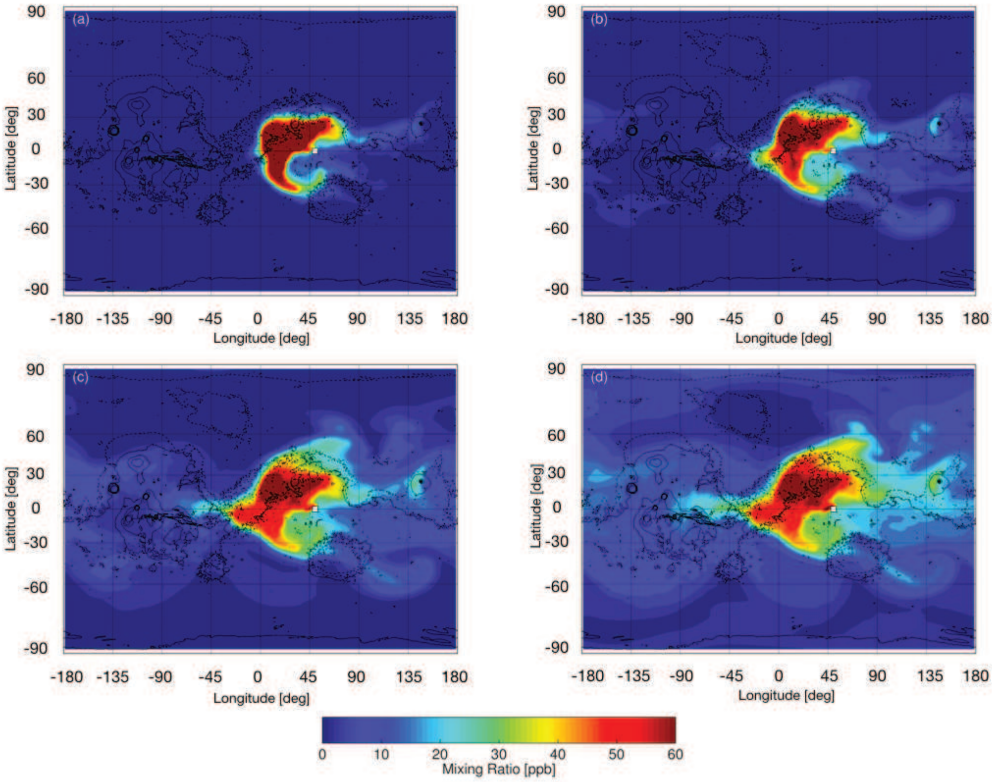

Fig. 6. Contours of column integrated methane mixing ratio for different release scenarios at the Iapygia II site (0°N, 50°E): (a) 15 sols, (b) 30 sols, (c) 45 sols, (d) 60 sols.

As noted before, the transport of a methane plume mainly depends on the wind in the boundary layer but, while the emitted methane is lifted by the vertical mixing and transported by the boundary layer winds, the near-surface layer winds still affect the transport of methane being injected as a result of the continuous emission. Fig. 5b shows high wind speeds close to the surface layer around the Iapygia region, up to 20 m/s, which enhances the meridional transport of the methane plume and eventually leads to the lifted methane being mixed and transported over a broad latitude range, as in the M09 observations. By contrast, as can be seen in Fig. 7e-f, for the cases where the emission is initiated in the nearby Iapygia region or the Aeolis region, a narrower latitudinal distribution of methane is obtained.

The effect of topography is observed on the transport of a methane plume. For the Coprates case, even though the methane plume is shifted westward, it is blocked by the high-elevation Tharsis formation, which prevents the methane plume from reaching to the Amazonis Planitia. Despite the methane plume extending far to the east, even reaching the M09 observation window, the methane concentration is quite low. However, the additional time allowed for latitudinal dispersion may produce methane distributions similar to the M09 observations, though a higher amount of methane would be needed to match the equatorial peak of methane concentration. The lowest methane concentrations in the M09 observation window are found for the emission from the Aeolis region, to the east.

Since the emission sites are located on the equator, the mid-latitude northern and southern hemisphere jets are not directly affecting the transport of the methane plume. However, after a given time period when the methane plume is transported in the meridional direction and vertically transported by convective mixing, methane distribution will be influenced by these two jets. Among all cases, the methane is least spread over the whole planet in the longitudinal direction for the Aeolis case. Moreover, as can be seen in Fig. 7a, when the emission is initiated at Arsia Mons, thanks to its high elevation, the methane plume is affected more by the stronger upper level winds. Accordingly, the zonal transport of the methane plume is strongest for this case, with a higher methane concentration in the Amazonis Planitia region than the Coprates case, which is the second strongest zonal transport.

The effect of elevation is also significant when the emission is initiated within the Coprates quadrangle. In Fig. 7b, it can be seen that the methane plume is transported zonally by the boundary layer winds but low concentration values are observed between [-120° E, -180° E] and [0° N, 45° N]. Even though the methane plume is transported from its source (-60° E) in the westward direction, the high concentration region which corresponds to the east of Tharsis region, does not extend to Amazonis Planitia, since the methane plume is not transported high enough to reach an altitude above Tharsis. In comparison, the concentration in the Amazonis Planitia region for the Sabaeous case is even lower, which is consistent given the conclusion drawn above. In addition, close to the Iapygia region, where the M09 observations were made, the meridional transport of methane is stronger than the Arsia Mons case. It is possible to relate this result to the high near-surface layer winds present close to the Iapygia region. Since the elevation of the release site is lower for the Coprates case with respect to the Arsia Mons case, within the same period, a larger amount of methane will stay close to the ground and will be therefore more affected by the near-surface layer winds. As a result of the low winds in the Coprates region, a higher methane concentration is found near the emission site in contrast to the Arsia Mons case. The effect of the boundary layer winds is significant in the eastward direction. As can be seen in Fig. 7c, the methane plume is centered close to its emission site, at 10° E, on the equator and is transported in two separate regions in the poleward direction, at 60° N and 40° S, and then zonally transported with the northern and southern hemisphere jets. Since the southern hemisphere jet is stronger than the northern one, the methane plume is transported further away in the southern hemisphere.

The other two emission locations are in the Iapygia region, and are referred to as Iapygia II and Iapygia. Even though these two emission sites are located

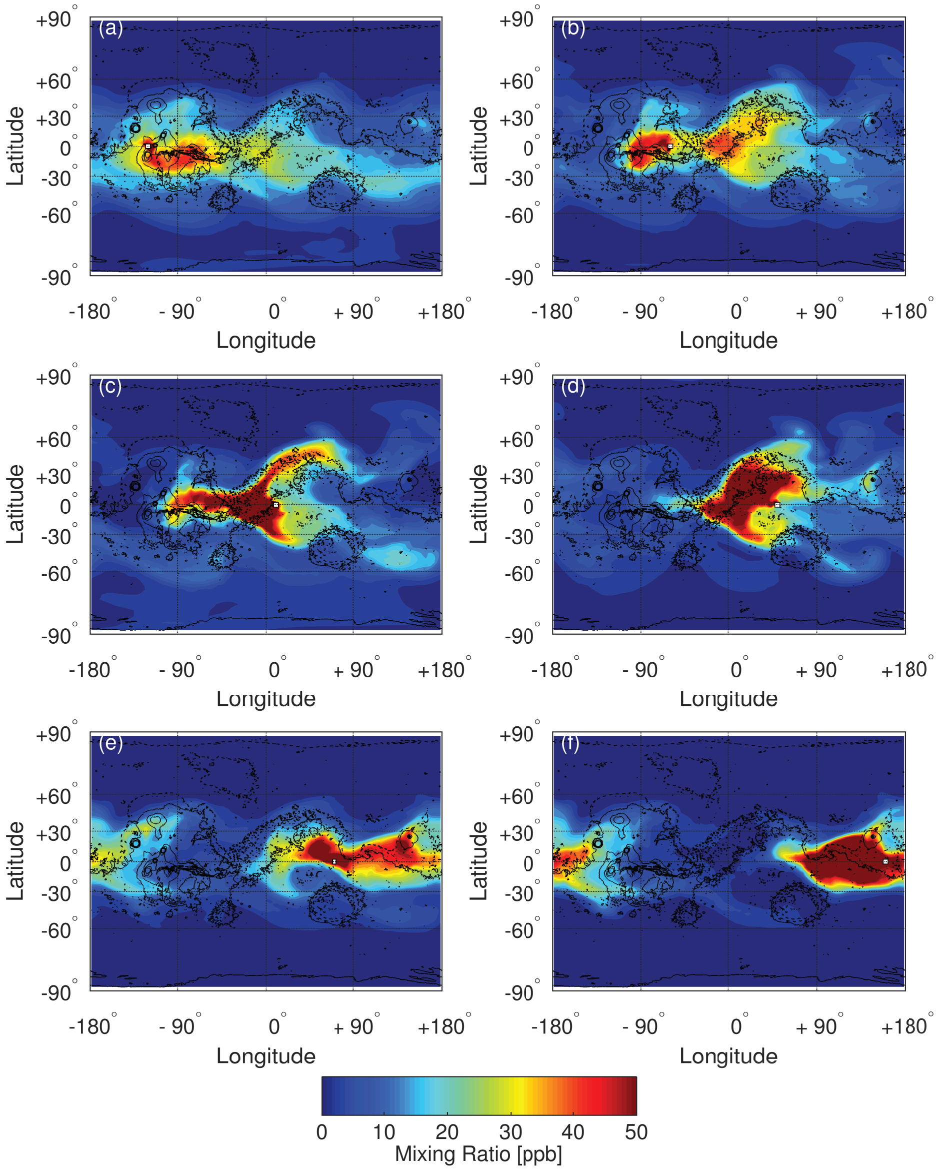

Fig. 7. Column integrated concentration of methane [ppb] contours for the emission scenario of 45 sols - $L_S = 155°$ (18 sols after the initial release) - Source locations: (a) Arsia Mons, (b) Coprates, (c) Sabaeous, (d) Iapygia II, (e) Iapygia, (f) Aeolis.

quite close and the winds on the lowest scale height are similar, the global variation of the column integrated methane concentration is different for both situations as can be seen in Fig. 7d and Fig. 7e. This can be explained with the wind field presented in Fig. 5b, which shows higher wind speeds close to the surface layer for the Iapygia II location, up to $\sim 20\ m/s$, blowing from south-east to north-west, compared to $\sim 5\ m/s$ for Iapygia, blowing from north-east to south-west. As a result, the methane is transported in the meridional direction within a latitude range of 100° for the Iapygia II case and a narrower distribution for the Iapygia location.

The last equatorial site considered is in the Aeolis region, where Gale crater is also located. As can be seen in Fig. 7f, the plume is mainly dispersed within Isidis Planitia (13° N, 87° E) and Elysium Planitia (3° N, 155° E) regions. However, due to the low wind speeds east of the Iapygia region, between 70° E and 100° E, on the equator, the plume is not transported further than Iapygia. Then, the methane plume is transported eastward through Amazonis Planitia (25° N, -170° E) by the boundary layer winds but, similar to the previous cases, the methane transport is limited by the topography of Alba Mons and Tharsis. Finally, in comparison to the Iapygia case, the methane concentration is higher to the south of Elysium Mons for the Aeolis case, which is due to the lower altitude of Aeolis emission site. Indeed, the higher elevation of the Iapygia region allows the methane plume to pass over the Elysium Mons, while its circulation is hampered in the Aeolis region leading to larger methane concentrations in that area.

In order to further investigate the methane transport within the Martian atmosphere, the meridional and zonal mean methane mixing ratio contours are given at $L_S = 155°$ for the emission scenario of 45 sols in Fig. 8 and Fig. 9 respectively. As shown in Fig. 8a and Fig. 9a, maximum vertical mixing is achieved for the Arsia Mons case, where the methane plume cannot be inhibited by any topographical features after it is lifted. Despite the fact that the release site in the Coprates region has a much lower elevation than Tharsis, similar results are obtained for this case as presented in Fig. 8b and Fig. 9b. The similarity between these two cases is that the methane is transported to a lower altitude than that from which it was initially emitted. The lifted methane is transported eastward with the boundary layer winds. As shown for the Arsia Mons case, when the methane is lifted and transported through a region where the elevation is lower, the transport of methane will be less affected by the topographical features so that the methane abundance will be higher well above the surface. Therefore, as for the Coprates case, the methane plume reaches a much higher altitude than the four other following cases.

As a consequence, the methane plume reaches a much higher altitude and is transported earlier by the boundary layer winds in the first two cases so that it is much more dispersed in the vertical direction as can be seen in Fig. 8a-b and Fig. 9a-b. For a surface release from the Sabaeous region, which is presented in Fig. 8c and Fig. 9c, methane concentrations are higher close to the ground and, consistent with the column integrated concentration contour given in Fig. 7c, the methane plume is transported to a higher latitude in the northern hemisphere. This can be explained by the same elevation effect as discussed for the Arsia Mons and Coprates cases. Since the elevation decreases in the northern direction, the effect of the global circulation on methane transport increases so that the methane plume reaches a higher latitude than it can reach in the southern hemisphere.

The final equatorial location being investigated is the Aeolis site, where methane is transported only to the east of Syrtis Major in the zonal direction. As can be seen in Fig. 8f, methane is first transported in the westward direction, through $120°E$ longitude, but then is mainly transported zonally by the boundary layer

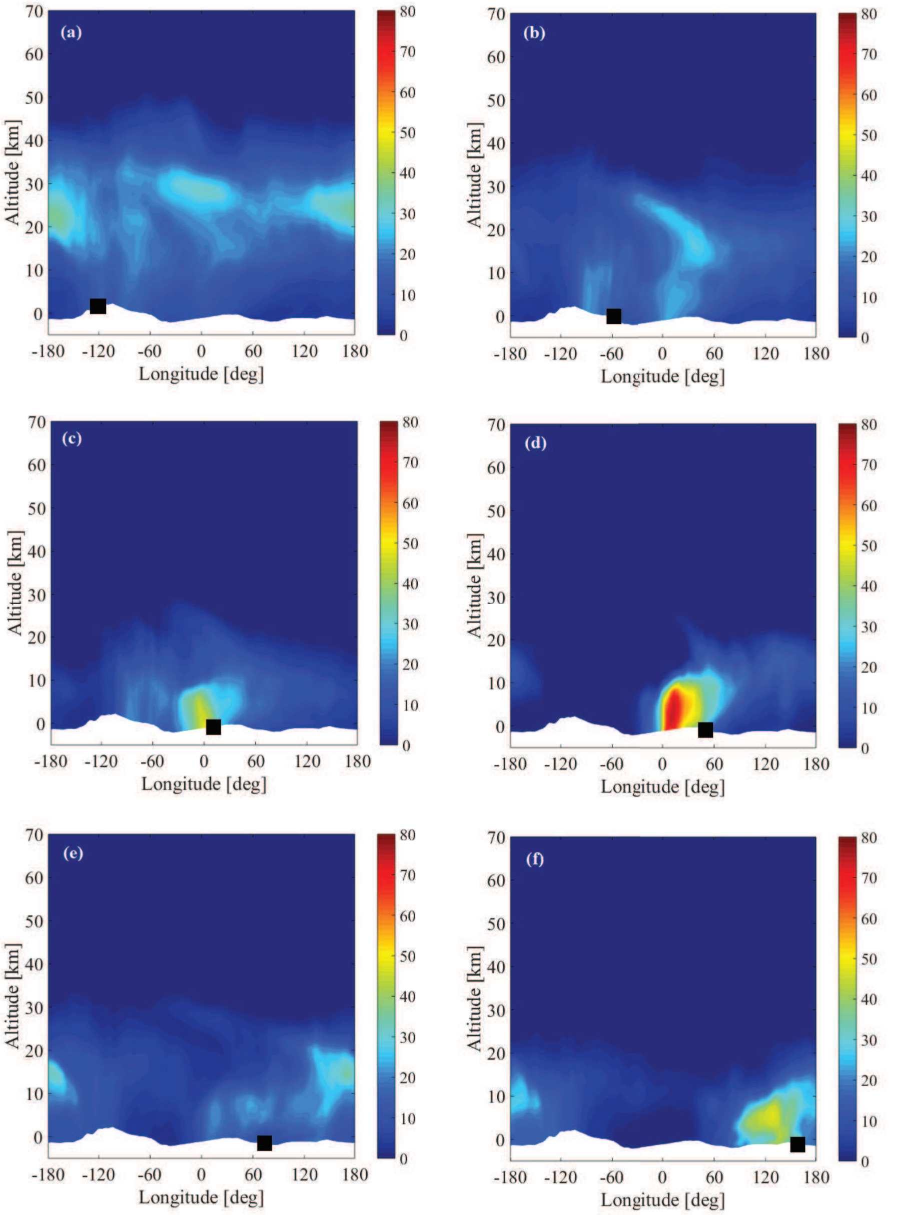

Fig. 8. Meridional mean methane mixing ratio [ppb] contours for the emission scenario of 45 sols - $L_S = 155°$ (18 sols after the initial release) - Source locations: (a) Arsia Mons, (b) Coprates, (c) Sabaeous, (d) Iapygia II, (e) Iapygia, (f) Aeolis.

winds through the west of Tharsis region.

The main scope of this study is to reproduce the M09 observations by using surface emissions of methane with a time-varying release rate. Hence, in order

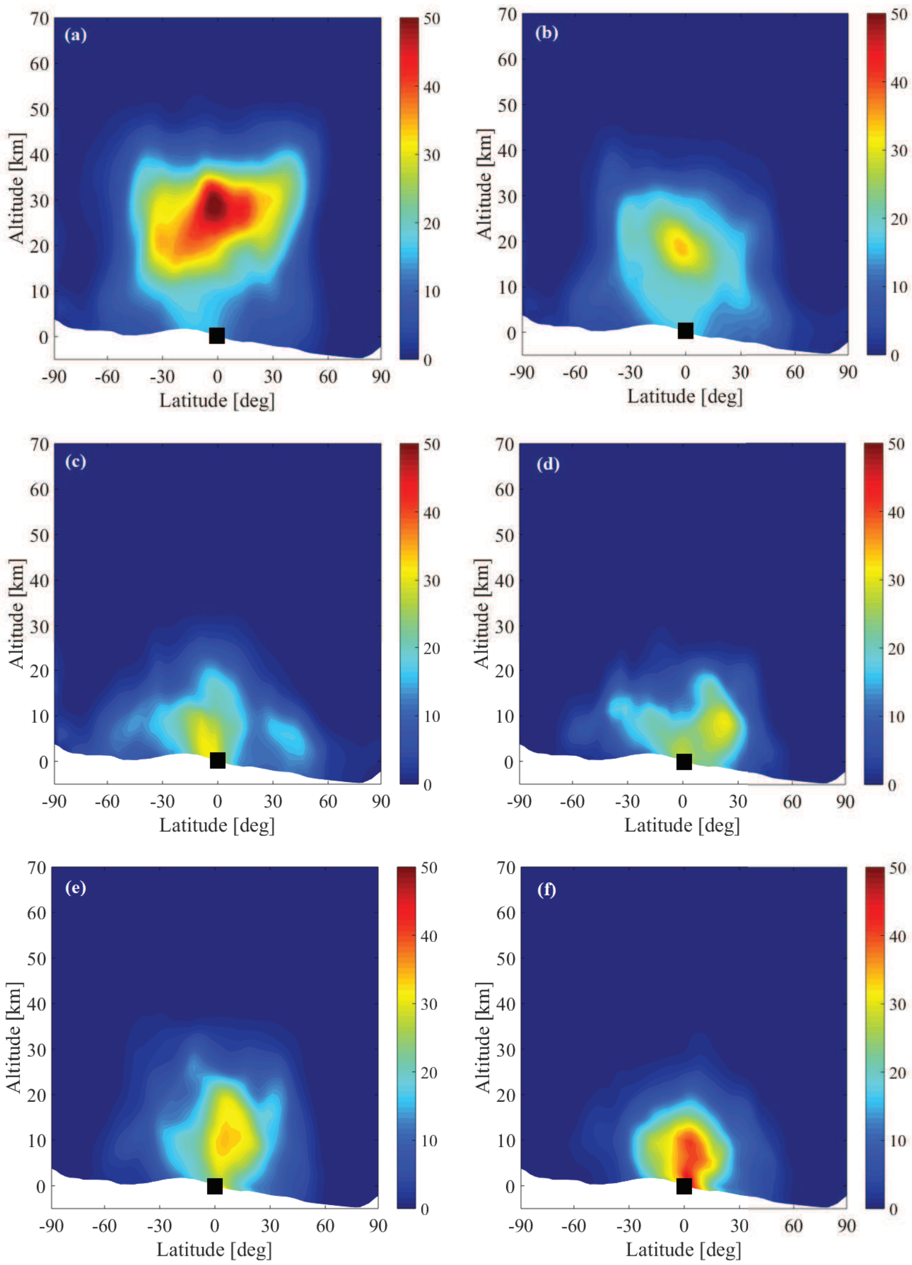

Fig. 9. Zonal mean methane mixing ratio [ppb] contours for the emission scenario of 45 sols - $L_S = 155°$ (18 sols after the initial release) - Source locations: (a) Arsia Mons, (b) Coprates, (c) Sabaeous, (d) Iapygia II, (e) Iapygia, (f) Aeolis.

to provide a quantitative evaluation of emission locations, the latitudinal distribution of the column integrated methane concentration in comparison to the M09 observations is given in Fig. 10, along with the hit rates presented in

Table 6. As noted before, at $L_S = 155.0°$, spatial averaging is performed on the longitudinal range of 32° E - 82° E, consistent with the M09 observations.

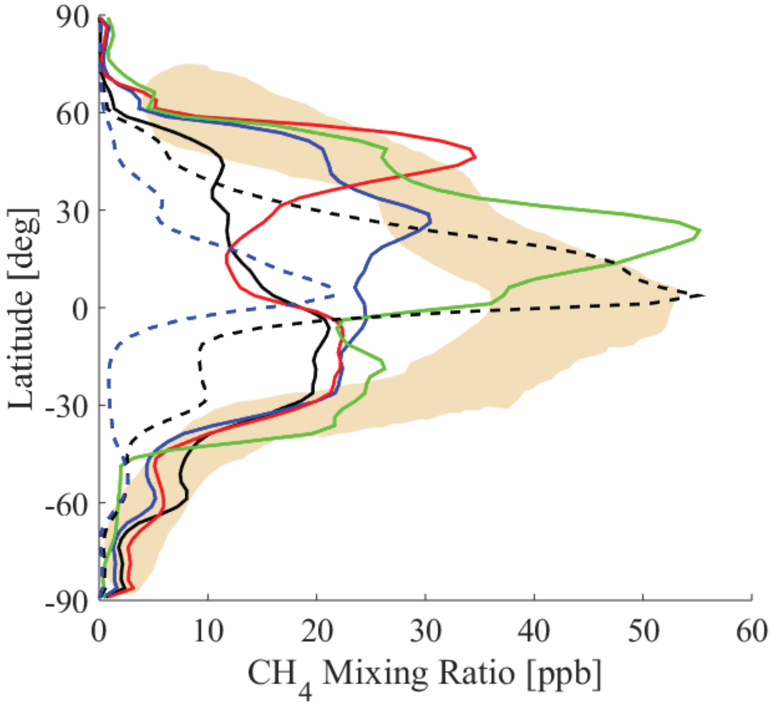

Fig. 10. Comparison of methane concentrations obtained for the emission scenario of 45 sols from the six different release sites on the equator with the M09 observations - $L_s = 155°$ (18 sols after the initial release) - spatially averaged over a longitudinal range of 32° E - 82° E. Black solid line: Arsia Mons, blue solid line: Coprates, red solid line: Sabaeous, green solid line: Iapygia II, black dashed line: Iapygia, blue dashed line: Aeolis, shaded area: M09 observations.

As expected, consistent with vertical and horizontal variation of methane mixing ratio for the Aeolis case shown in Fig. 7f, Fig. 8 and Fig. 9, the lowest methane concentrations are computed for the case where the release site is located within Aeolis region. Arsia Mons, although being the furthest site from the M09 observation region, shows a profile where methane mixing ratios are larger than in the Aeolis case. This is explained by the high elevation of Tharsis which allows methane to be transported by the general circula-

Table 6

Intercomparison of equatorial emission scenarios of 45 sols to reproduce the M09 observations

Emission location	**Hit rate [%]**
Tharsis	46.2
Coprates	60.0
Sabaeous	49.2
Iapygia II	59.0
Iapygia	21.5
Aeolis	6.2

tion earlier than when it is emitted from the Aeolis site. For the Sabaeous case, despite methane concentrations close to the observed quantities in the mid-latitudes, the computed values on the equator are lower than the ones in the Aeolis case. For the Coprates case, the methane is emitted 70° west of the Sabaeous site. In other words, in terms of the distance to the spatial range of M09 observations, the Coprates emission site is located much further away than the Sabaeous site. Despite this fact, better estimations of the latitudinal distribution of methane mixing ratio are obtained in that case in terms of comparison with the M09 observations. The Iapygia case provides a good agreement with the observations close to the equator but the meridional spreading of the methane plume is under-estimated. In comparison, the methane emission from Iapygia II provides a much better agreement in the mid-latitudes. However, there is a meridional shift in the latitude where the methane concentration reaches its maximum value, which points out the importance of investigating the effect of the meridional position of the emission to reproduce the M09 observations. As presented in Table 6, the results of the Coprates and Iapygia II cases are similar in terms of hit rate calculations.

The Coprates case provides an under-estimated methane concentration estimation on the equator. Therefore, it is possible to state that the Iapygia II case provided better results than the Coprates case. Finally, it must be noted that if the total amount of emitted methane is further increased, it is also possible to match M09 observations for different cases. However, since a reasonable agreement with the M09 observations is found out to be possible for the Iapygia II case with the minimum amount of methane, with the longest possible chemical life time, it is concluded that Iapygia II region provides the best agreement with the observations.

4.3 Sensitivity to the meridional position of the surface release

Following the conclusion that, among the equatorial release sites tested, the Iapygia II region provides the best agreement with the M09 observations, four additional emission locations, given in Table 4, are investigated on the same longitude of the Iapygia II case. The methane mixing ratios obtained at $L_S = 155°$ for these four new sites with the emission scenario of 45 sols are presented in Fig. 11 along with the results of the Iapygia II case and the M09 observations. The hit rate calculations are also given in Table 7 to present a quantitative comparison.

Table 7 shows that the best results are obtained for the Iapygia II-S1 case. As expected, the further north the emission is initiated, the greater the underestimation of the methane concentration in the southern hemisphere. Moreover, the overestimation of the methane concentration in the northern hemisphere increases. Unlike this monotonic behavior for the northern releases in the Iapygia region, when methane is released in a southern location, instead of a single

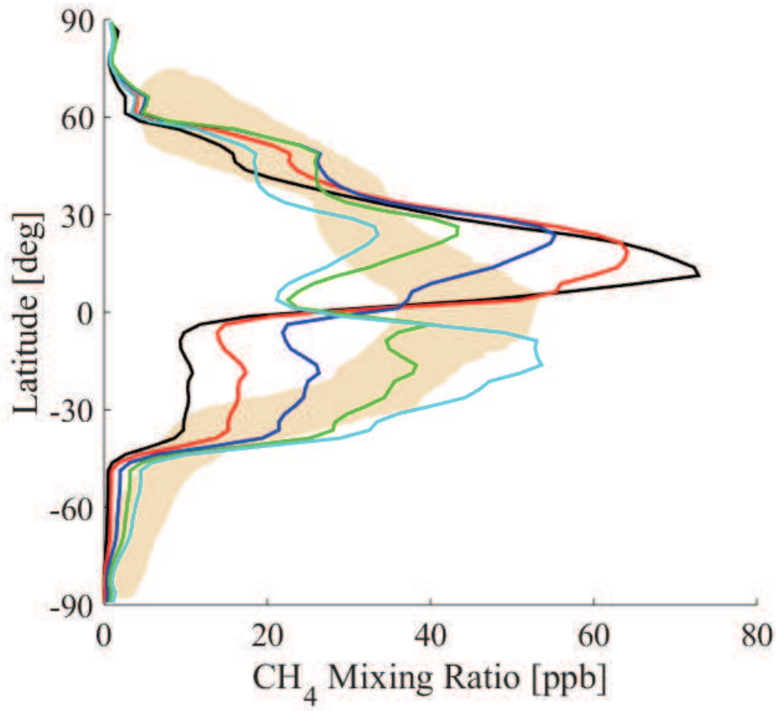

Fig. 11. Comparison of methane concentrations for different release location along the latitude of Iapygia II. The figure shows results obtained for the emission scenario of 45 sols from different emission locations with M09 observations - $L_s = 155°$ (18 sols after the initial release). Black solid line: Iapygia II - N2, red solid line: Iapygia II - N1, blue solid line: Iapygia II, green solid line: Iapygia II - S1, cyan solid line: Iapygia II - S2, shaded area: M09 observations.

Table 7

Intercomparison of Iapygia II cases to reproduce the M09 observations

Emission location	**Hit rate** [%]
Iapygia II - S2	53.8
Iapygia II - S1	69.2
Iapygia II	59.0
Iapygia II - N1	27.7
Iapygia II - N2	20.0

methane concentration peak close to the equator, two peaks are obtained in the northern and southern hemispheres. This behavior is related to the bidirectional winds close to the release locations for the Iapygia II - S2 and Iapygia II - S1 cases, (see Fig. 5).

Temporal evolution of the methane plume of the emission scenario of 45 sols initiated at Iapygia II - S1 is investigated in Fig. 12 and Fig. 13, which presents the column integrated methane mixing ratio and zonal/meridional mean methane mixing ratio contours for different time periods. Within the first 10 sols (Fig. 12a and Fig. 12b), the methane plume is transported the north-west direction consistently with the winds presented in Fig. 5a. Zonal and meridional mean methane mixing ratio contours 10 sols after the initial emission in Fig. 13a-b show that the methane plume is not yet vertically lofted high enough to be transported by the stronger upper winds. As can be seen in Fig. 13c-f, after 15-20 sols, the methane plume is lifted well above and then transported by the boundary layer winds, leading the plume through the east direction as shown in Fig. 12c and Fig. 12d. Fig. 12e-f exposes the effect of the high elevation in the Tharsis region, where the lowest concentration values are obtained close to the equator. Considering that the atmospheric mass equals 2.4×10^{16} kg (Withers, 2012) and the total amount of methane is set to 8.99×10^{7} kg, a global mean mixing ratio of $\sim$11 ppb would be obtained if uniformly mixed over the planet. Consistently, the column integrated methane mixing ratio contours (Fig. 12f) show a mean methane mixing ratio of $\sim$20 ppb in the mid-latitudes and, down to $\sim$1 ppb away from the mid-latitudes.

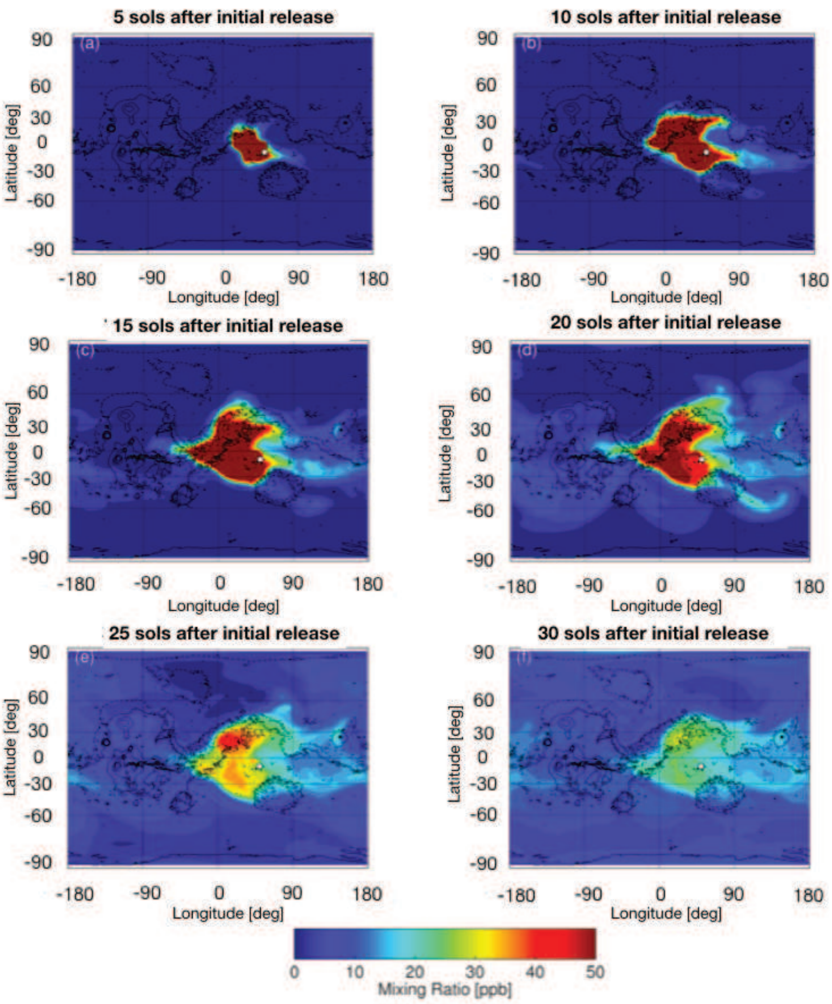

Fig. 12. Column integrated methane mixing ratio [ppb] contours for the emission scenario of 45 sols - Iapygia II - S1: (a)-5 sols, (b)-10 sols, (c)-15 sols, (d)-20 sols, (e)-25 sols, (f)-30 sols after initial release.

5 Discussion

In this study, different emission scenarios, ranging from 15 sols of emission duration to 60 sols, initiated from different locations are investigated. Considering the relatively short simulation duration with respect to methane photochemical lifetime (Lefèvre and Forget, 2009), the GCM is not coupled with chemistry, as with most similar studies (Viscardy et al., 2016; Mischna et al.,

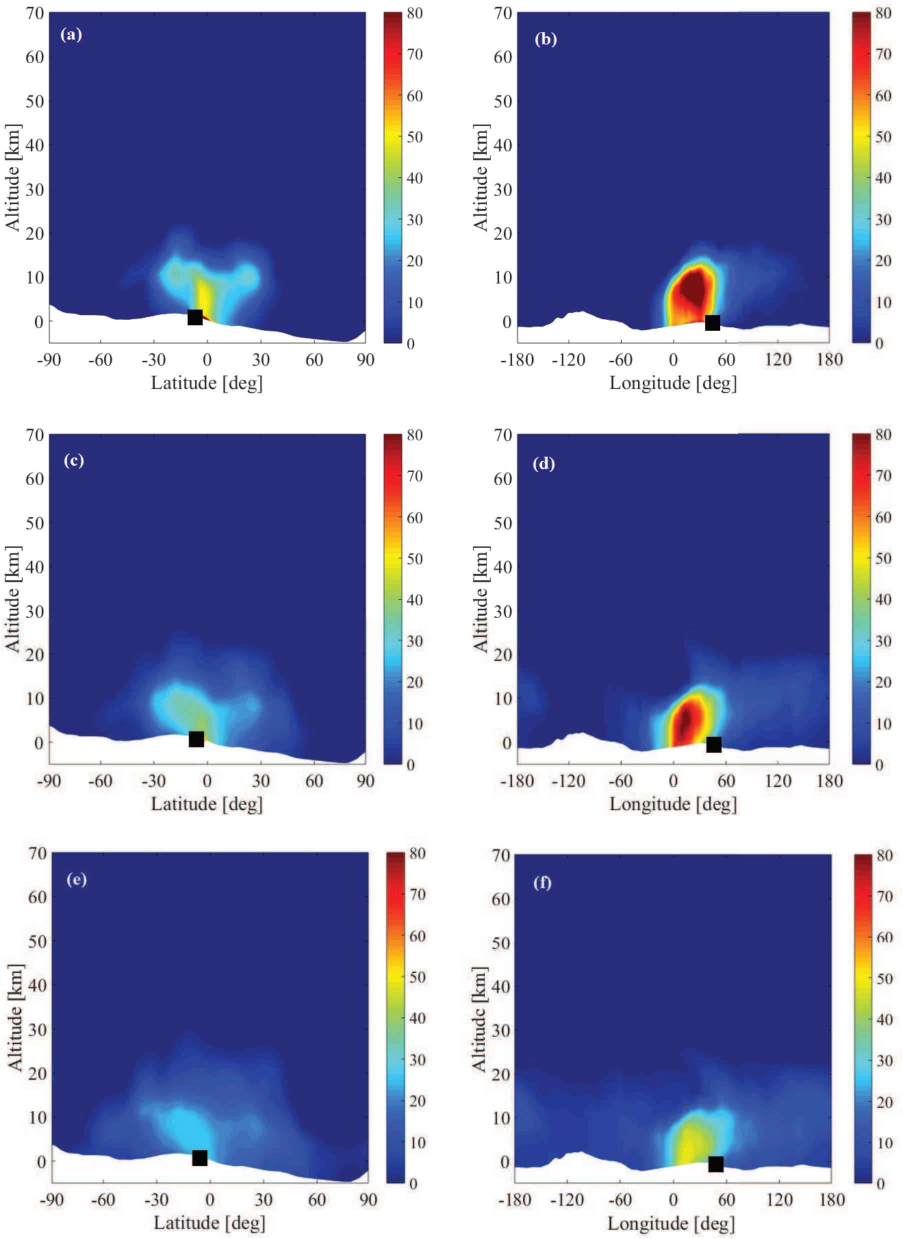

Fig. 13. Zonal and meridional mean methane mixing ratio [ppb] contours for the emission scenario of 45 sols - Iapygia II - S1: (a,b)-10 sols, (c,d)-15 sols, (e,f)-20 sols after initial release.

2011; Holmes et al., 2015). Therefore, for long-term simulations, when the remaining methane would be convected well above our present upper boundary (∼80 km), the applicability of our methodology is open to question.

The total amounts of methane for the emission scenarios of 60, 45, 30 and 15 sols correspond to a global methane mixing ratio of 15, 11, 7, 5 ppb. These numbers, especially those with shorter emission durations, are similar to the global mean mixing ratio of 6 ppb (or 42,000 tons), reported for the entire region mapped during M09 observations. Considering that only 3 ppb of methane had been observed in 2006 early spring equinox after the M09 observations in 2003, these global methane mixing ratio values correspond to an approximate chemical lifetime of ∼700, ∼800, ∼1300 and ∼2200 sols for the emission scenarios of 60, 45, 30 and 15 sols, respectively. The estimated chemical lifetimes are close to the destruction lifetime which was used in one of the previous studies (Mischna et al., 2011) and those reported by M09, much shorter than the time scales estimated for photochemical destruction (Lefèvre and Forget, 2009). Hence, the present study, similar to previous ones, indicates to an unknown sink, much more efficient than the atmospheric photochemistry by at least two order of magnitudes.

The results and the related discussions on the different emission scenarios have shown that the methane plume is not transported enough in the meridional direction to match the M09 observations for the case of a short emission duration. On the other hand, the amount of methane released in the Martian atmosphere needs to be properly increased for longer emission duration in order to obtain a mixing ratio of ∼40 ppb close to the equator. This is problematic because increasing the total quantity of methane implies a faster destruction mechanism. Indeed, methane release lasting more than 60 sols requires a destruction lifetime shorter than 700 sols. Therefore, it leads to the conclusion that in the case of a singular source with the known photochemistry mechanisms, neither an instantaneous or a short-time sub-surface release, nor a long-term sub-surface methane release can be the source of the methane abundance reported during M09 observations.

The GCM model was not fully coupled with the subsurface transport model, which determined the surface fluxes independently. It can be regarded only as a one-way, weakly coupled model considering the fact that a generic release scenario is used despite the subsurface model parameters and the fact that the resulting methane flux actually depends on the temporally and spatially varying surface temperature and pressure. The subsurface transport model is considered to be purely diffusive. Additional effects such as advection, thermal transpiration, baro-diffusion, etc. are not taken into account considering the uncertainties in the subsurface properties. A comprehensive sensitivity analysis of subsurface transport model to model parameters is the subject of a subsequent paper.

The shallow depth of the methane sources revealed in this study, are consistent with the observed temporal variations and localized sources (Lefèvre and Forget, 2009; Mumma et al., 2009). If abiotic, the origin could be due the destabilization of a localized layer of zeolites (Mousis et al., 2016) or clathrates (Chastain and Chevrier, 2007). Mousis et al. (2016) suggested that the presence of zeolites minerals observed around Gale crater could explain the variation of the methane level observed by MSL although they are most likely formed at much deeper depths ranging from approximately 8 to 15, 20 km. Clathrates are thermodynamically stable in the Martian subsurface at depths depending on the soils properties. The estimated upper bound of a pure methane clathrate stability zone in the equatorial region of Mars is $\sim$45 m (Root and Elwood Madden, 2012). The sources considered in this study are at depths of the same order of magnitude, although slightly shallower. The addition of

CO_2 in methane clathrate hydrates decreases the dissociation pressure for the same temperature conditions, allowing them to be stable at shallower depths. On the other hand, near-surface clathrate hydrates destabilized by obliquity changes may be preserved over geologic time scales as metastable reservoirs (Root and Elwood Madden, 2012). These methane reservoirs could thus be located outside their present-day stability zone in the Martian subsurface at depths, closer to the surface, corresponding to past stability zones associated with larger obliquities and colder surface temperatures at the equator of the planet.

A potential analog for methane surface releases on Mars is methane emissions from Arctic tundra on Earth (Mastepanov et al., 2008; Pirk et al., 2015; Zona et al., 2016), although the origin and transport mechanism may show significant differences. Arctic permafrost underlying wetlands, constitute a large source of methane, which is produced by microorganisms in the seasonally unfrozen layer of the soil and transported to the surface by diffusion through the soil pore spaces, by plant-mediated transport through aerenchyma of vascular plants or convectively by sudden ebullition events. The mean surface fluxes obtained in the present study, on the order of 3-5 mg m^{-2} h^{-1}, are comparable to the seasonal emissions observed in the Arctic tundra, up to 2 mg m^{-2} h^{-1} (Zona et al., 2016). In the Arctic, peak emissions up to 112.5 mg m^{-2} h^{-1} were detected over measurement chambers (Mastepanov et al., 2008), whereas the peak surface fluxes reaches to $\sim$ 30 mg m^{-2} h^{-1} in the present study. The average methane release flux considered in the present study, in the order of $\sim$ 31 - 21 kg s^{-1}, corresponding to $\sim$ 1.0 - 0.6 Tg y^{-1} annually, which is smaller than the observed global annual methane release rate from the Arctic (23 $\pm$ 8 Tg y^{-1}, Zona et al. (2016)) but slightly larger than the yearly geochemical production of methane by serpentinization (0.05 - 0.13 Tg y^{-1} along the entire Mid-Atlantic Ridge on Earth, Lefèvre and Forget (2009)). For another comparison, the massive hydrocarbon seep field at Coal Oil Point in Santa Barbara, California, releases 12,000 - 30,000 metric ton of methane (Mau et al., 2007), which is on the same order of magnitude for the emission scenario of 15 sols (40,000 metric ton).

We considered several locations to test the sensitivity of the results to release locations. The results have shown the importance of the topography at the emission location including the elevation and the complexity of the terrain. It has been found that with higher elevations, the methane plume spreads faster within the atmosphere, and it is also possible to claim that variations in the wind direction may also increase the spreading of the plume.

Our objective has not been to constrain the exact source location, which would require more simulations and likely to be challenging considering the difficulties of constraining the models and observations considering their uncertainties (Holmes et al., 2015; Lefèvre and Forget, 2009) but, rather to highlight the impact of the topography on the evolution of a gas plume and investigate the effect of the depth of a subsurface source on the transport of methane. In addition, for source regions where the effect of topography is too complex for a GCM, like Gale crater (Rafkin et al., 2016), mesoscale simulations might need to be performed for realistic modeling of the methane plumes. Despite this fact, our results have shown the potential of GCM simulations, sustained with the surface methane flux from a subsurface model to predict the methane plumes. It must also be noted that observations more detailed than M09 are needed to determine the exact location of release location. For instance, the ExoMars Trace Gas Orbiter (TGO) mission consists of two instruments to perform limb and nadir measurements of trace gases within the Martian atmosphere, so both the horizontal and vertical distributions of methane are investigated. Therefore, a possible future study can be the application of GCM/subsurface model coupling, or even mesoscale simulations depending on the terrain complexity of release location, to reproduce TGO measurements.

6 Conclusions

In this study, we tested different methane emission scenarios on Mars by considering different source regions and emission durations. Methane from hypothetical subsurface sources is injected into the atmosphere based on a subsurface gas transport model. The methane transport in the Mars atmosphere is then simulated using a general circulation model, MarsWRF. The results have shown that methane surface releases determined by a subsurface transport model can reproduce the M09 observations to a better degree of accuracy than previous studies (Mischna et al., 2011). Among the emission locations and durations tested, it is found that an emission scenario of 45 sols, initiated from the Iapygia region (50° E, 10° S), provided the best agreement with the M09 observations, in terms of producing the latitudinal mixing of the methane plume with a slightly larger amount of methane than the one estimated by (Mumma et al., 2009). The results of the Iapygia II case with different meridional locations show that when the methane is released away from the equator, at 20° N or 20° S, the predicted methane concentration deviates from the M09 observations. In the case of multiple sources, it might be possible to obtain better results in comparison to the M09 observations, but for a single subsurface source as tested here, our findings show that a source close to the equator provides a better fit to the observations than a source at higher latitudes.

Following the discussion stated in Section 5, the horizontal and vertical distribution of a methane plume is investigated during the methane emission from the surface. The results have shown the importance of topography on the transport of a methane plume, originated from a subsurface, time-varying source. When the emission is initiated from an emission site with a higher elevation, such as the Arsia Mons case, the methane plume is affected more by the stronger upper level winds, leading to a stronger zonal transport. Moreover, we tested emission scenarios, corresponding to different subsurface source depths. Among these scenarios, the best agreement with the M09 observations is obtained by using a subsurface source located at a depth of $\sim$27 m. Our results have also shown that a vertical gradient of methane will exist during an emission. Therefore, it is possible to conclude that a vertical gradient points an active release and a uniform methane distribution within the boundary layer might suggest an older source.

Finally, in situ methane measurements of the Curiosity rover are ongoing at Gale crater in addition to ongoing observations of the ExoMars TGO. If another strong release of methane similar to the one during M09 observations were reported, it would be a good case to validate the current methodology and improve the proposed scenario.

Acknowledgements

This work was financially supported by the Belgian Science Policy Office (BELSPO) through the Interuniversity Attraction Poles Program Planet Topers, the BRAIN-be Program SCOOP and the ESA/PRODEX Program. It received funding from the European Unions Horizon 2020 Program (H2020-Compet-08-2014) under grant agreement UPWARDS-633127. A portion of this work was performed at the Jet Propulsion Laboratory, California Institute of Technology, under a contract with NASA. Authors would like to acknowledge to Dr. Luca Montabone, from Space Science Institute (SSI), Boulder, CO, USA, for providing the surface temperature observations acquired by Thermal Emission Spectrometer (TES). We are also grateful to two anonymous reviewers who helped to clarify the story and provided excellent feedback.

References

Boston, P. J., Ivanov, M. V., McKay, C. P., 1992. On the possibility of chemosynthetic ecosystems in subsurface habitats on Mars. Icarus 95 (2), 300–308.

Chassefière, E., 2009. Metastable methane clathrate particles as a source of methane to the martian atmosphere. Icarus 204 (1), 137–144.

Chastain, B. K., Chevrier, V., 2007. Methane clathrate hydrates as a potential source for martian atmospheric methane. Planetary and Space Science 55 (10), 1246–1256.

Elwood Madden, M., Ulrich, S. M., Onstott, T., Phelps, T. J., 2007. Salinity-induced hydrate dissociation: A mechanism for recent CH_4 release on Mars. Geophysical research letters 34 (11).

Formisano, V., Atreya, S., Encrenaz, T., Ignatiev, N., Giuranna, M., 2004. Detection of methane in the atmosphere of Mars. Science 306 (5702), 1758–1761.

Geminale, A., Formisano, V., Giuranna, M., 2008. Methane in Martian atmosphere: average spatial, diurnal, and seasonal behaviour. Planetary and Space Science 56 (9), 1194–1203.

Guo, X., Lawson, W. G., Richardson, M. I., Toigo, A., 2009. Fitting the Viking lander surface pressure cycle with a Mars General Circulation Model. Journal of Geophysical Research: Planets 114 (E7).

Holmes, J., Patel, M., Lewis, S., 2017. The vertical transport of methane from different potential emission types on Mars. Geophysical Research Letters 44 (16), 8611–8620.

Holmes, J. A., Lewis, S. R., Patel, M. R., 2015. Analysing the consistency of martian methane observations by investigation of global methane transport. Icarus 257, 23–32.

Kite, E. S., Gao, P., Goldblatt, C., Mischna, M. A., Mayer, D. P., Yung, Y. L., 2017. Methane bursts as a trigger for intermittent lake-forming climates on post-Noachian Mars. Nature Geoscience 10 (10), 737.

Krasnopolsky, V. A., Maillard, J. P., Owen, T. C., 2004. Detection of methane in the martian atmosphere: evidence for life? Icarus 172 (2), 537–547.

Kress, M. E., McKay, C. P., 2004. Formation of methane in comet impacts: implications for Earth, Mars, and Titan. Icarus 168 (2), 475–483.

Lasue, J., Quesnel, Y., Langlais, B., Chassefière, E., 2015. Methane storage capacity of the early Martian cryosphere. Icarus 260, 205–214.

Lee, C., Lawson, W., Richardson, M., Anderson, J., Collins, N., Hoar, T., Mischna, M., 2011. Demonstration of ensemble data assimilation for Mars using DART, MarsWRF, and radiance observations from MGS TES. Journal of Geophysical Research: Planets 116 (E11).

Lee, C., Lawson, W., Richardson, M., Heavens, N., Kleinböhl, A., Banfield, D., McCleese, D., Zurek, R., Kass, D., Schofield, J., et al., 2009. Thermal tides in the Martian middle atmosphere as seen by the Mars Climate Sounder.

Journal of Geophysical Research: Planets 114 (E3).

Lee, C., Richardson, M., Newman, C., Toigo, A., 2006. VenusWRF: A New Venus GCM Using PlanetWRF. In: Bulletin of the American Astronomical Society. Vol. 38. p. 526.

Lefèvre, F., Forget, F., 2009. Observed variations of methane on Mars unexplained by known atmospheric chemistry and physics. Nature 460 (7256), 720–723.

Lyons, J. R., Manning, C., Nimmo, F., 2005. Formation of methane on Mars by fluid-rock interaction in the crust. Geophysical Research Letters 32 (13).

Mastepanov, M., Sigsgaard, C., Dlugokencky, E. J., Houweling, S., Ström, L., Tamstorf, M. P., Christensen, T. R., Dec. 2008. Large tundra methane burst during onset of freezing. Nature 456 (7222), 628–630.

Mau, S., Valentine, D., Clark, J., Reed, J., Camilli, R., Washburn, L., 2007. Dissolved methane distributions and airsea flux in the plume of a massive seep field, Coal Oil Point, California. Geophysical Research Letters 34, no. 22.

Max, M. D., Clifford, S. M., 2000. The state, potential distribution, and biological implications of methane in the Martian crust. Journal of Geophysical Research: Planets 105 (E2), 4165–4171.

McDonald, G. D., Hayes, A. G., Ewing, R. C., Lora, J. M., Newman, C. E., Tokano, T., Lucas, A., Soto, A., Chen, G., 2016. Variations in Titan's dune orientations as a result of orbital forcing. Icarus 270, 197–210.

Mischna, M., Wilson, R., 2008. The mars general circulation model intercomparison study. LPI Contributions 1447, 9088.

Mischna, M. A., Allen, M., Richardson, M. I., Newman, C. E., Toigo, A. D., 2011. Atmospheric modeling of Mars methane surface releases. Planetary and Space Science 59 (2), 227–237.

Mousis, O., Chassefière, E., Lasue, J., Chevrier, V., Elwood Madden, M. E., Lakhlifi, A., Lunine, J. I., Montmessin, F., Picaud, S., Schmidt, F., et al., 2013. Volatile trapping in Martian clathrates. Space Science Reviews 174 (1-4), 213–250.

Mousis, O., Simon, J.-M., Bellat, J.-P., Schmidt, F., Bouley, S., Chassefière, E., Sautter, V., Quesnel, Y., Picaud, S., Lectez, S., 2016. Martian zeolites as a source of atmospheric methane. Icarus 278, 1–6.

Mumma, M. J., Villanueva, G. L., Novak, R. E., Hewagama, T., Bonev, B. P., DiSanti, M. A., Mandell, A. M., Smith, M. D., 2009. Strong release of methane on Mars in northern summer 2003. Science 323 (5917), 1041–1045.

Mustard, J., Ehlmann, B., Murchie, S., Poulet, F., Mangold, N., Head, J., Bibring, J.-P., Roach, L., 2009. Composition, morphology, and stratigraphy of Noachian crust around the Isidis basin. Journal of Geophysical Research: Planets 114 (E2).

Mustard, J., Poulet, F., Head, J., Mangold, N., Bibring, J.-P., Pelkey, S., Fassett, C., Langevin, Y., Neukum, G., 2007. Mineralogy of the Nili Fossae region with OMEGA/Mars Express data: 1. Ancient impact melt in the Isidis Basin and implications for the transition from the Noachian to Hesperian. Journal of Geophysical Research: Planets 112 (E8).

Oehler, D. Z., Etiope, G., 2017. Methane seepage on Mars: where to look and why. Astrobiology 17 (12), 1233–1264.

Oze, C., Sharma, M., 2005. Have olivine, will gas: Serpentinization and the abiogenic production of methane on mars. Geophysical Research Letters 32 (10).

Parro, L. M., Jiménez-Díaz, A., Mansilla, F., Ruiz, J., 2017. Present-day heat flow model of Mars. Scientific reports 7, 45629.

Petrosyan, A., Galperin, B., Larsen, S. E., Lewis, S., Määttänen, A., Read, P., Renno, N., Rogberg, L., Savijärvi, H., Siili, T., et al., 2011. The Martian atmospheric boundary layer. Reviews of Geophysics 49 (3).

Pirk, N., Santos, T., Gustafson, C., Johansson, A., Tufvesson, F., Parmentier, F., Mastepanov, M., Christensen, T., 2015. Methane emission bursts from permafrost environments during autumn freezein: New insights from groundpenetrating radar. Geophysical Research Letters 42.16, 6732–6738.

Rafkin, S., Pla-Garcia, J., Kahre, M., G.-E. J., Hamilton, V., Marn, M., Navarro, S., Torres, J., Vasavada, A., 2016. The meteorology of Gale Crater as determined from Rover Environmental Monitoring Station observations and numerical modeling. Part II: Interpretation. Icarus 280, 114–138.

Richardson, M. I., Toigo, A. D., Newman, C. E., 2007. PlanetWRF: A general purpose, local to global numerical model for planetary atmospheric and climate dynamics. Journal of Geophysical Research: Planets 112 (E9).

Root, M. J., Elwood Madden, M. E., 2012. Potential effects of obliquity change on gas hydrate stability zones on Mars. Icarus 218 (1), 534–544.

Sizemore, H. G., Mellon, M. T., 2008. Laboratory characterization of the structural properties controlling dynamical gas transport in Mars-analog soils. Icarus 197 (2), 606–620.

Smith, M. D., Pearl, J. C., Conrath, B. J., Christensen, P. R., 2001. One Martian year of atmospheric observations by the Thermal Emission Spectrometer. Geophysical research letters 28 (22), 4263–4266.

Stevens, A. H., Patel, M. R., Lewis, S. R., Jan. 2017. Modelled isotopic fractionation and transient diffusive release of methane from potential subsurface sources on Mars. Icarus 281 (C), 240–247.

Toigo, A. D., French, R. G., Gierasch, P. J., Guzewich, S. D., Zhu, X., Richardson, M. I., 2015. General circulation models of the dynamics of Pluto's volatile transport on the eve of the New Horizons encounter. Icarus 254, 306–323.

Toigo, A. D., Lee, C., Newman, C. E., Richardson, M. I., 2012. The impact of resolution on the dynamics of the martian global atmosphere: Varying resolution studies with the MarsWRF GCM. Icarus 221 (1), 276–288.

Viscardy, S., Daerden, F., Neary, L., 2016. Formation of layers of methane in the atmosphere of Mars after surface release. Geophysical Research Letters 43 (5), 1868–1875.

Webster, C. R., Mahaffy, P. R., Atreya, S. K., Flesch, G. J., Mischna, M. A., Meslin, P.-Y., Farley, K. A., Conrad, P. G., Christensen, L. E., Pavlov, A. A., et al., 2015. Mars methane detection and variability at Gale crater. Science 347 (6220), 415–417.

Webster, C. R., Mahaffy, P. R., Atreya, S. K., Moores, J. E., Flesch, G. J., Malespin, C., McKay, C. P., Martinez, G., Smith, C. L., Martin-Torres, J., et al., 2018. Background levels of methane in Mars' atmosphere show strong seasonal variations. Science 360 (6393), 1093–1096.

Weiss, B. P., Yung, Y. L., Nealson, K. H., 2000. Atmospheric energy for subsurface life on Mars? Proceedings of the National Academy of Sciences 97 (4), 1395–1399.

Welty, J. R., Wicks, C. E., Rorrer, G., Wilson, R. E., 2009. Fundamentals of momentum, heat, and mass transfer. John Wiley & Sons.

Withers, P., 2012. Empirical estimates of Martian surface pressure in support of the landing of Mars Science Laboratory. Space science reviews 170.1-4, 837–860.

Zahnle, K., 2015. Play it again, SAM. Science 347 (6220), 370–371.

Zahnle, K., Freedman, R. S., Catling, D. C., 2011. Is there methane on Mars? Icarus 212 (2), 493–503.

Zona, D., Gioli, B., Commane, R., Lindaas, J., Wofsy, S. C., Miller, C. E., Dinardo, S. J., Dengel, S., Sweeney, C., Karion, A., Chang, R. Y. W., Henderson, J. M., Murphy, P. C., Goodrich, J. P., Moreaux, V., Liljedahl, A., Watts, J. D., Kimball, J. S., Lipson, D. A., Oechel, W. C., Jan. 2016. Cold season emissions dominate the Arctic tundra methane budget. Proceedings of the National Academy of Sciences of the United States of America 113 (1), 40–45.